Investigation of Shubnikov–de Haas oscillations in a crystalline topological insulator SnTe/$Sn_{1-x}Eu_xTe$ heterostructure

I. F. Costa,[1] U. A. Mengui,[2] E. Abramof,[2] P. H. O. Rappl,[2] D. A. W. Soares,[2] S. de Castro,[3] and M. L. Peres[1,*]

[1]*Instituto de Física e Química, Universidade Federal de Itajubá, Itajubá, CEP 37500-903, Minas Gerais, Brazil*

[2]*Grupo de Pesquisa e Desenvolvimento em Materiais e Plasma - GPDMP, Instituto Nacional de Pesquisas Espaciais, São José dos Campos, CEP 12201-970, São Paulo, Brazil*

[3]*Universidade do Estado de Minas Gerais, Divinópolis, CEP 35501-170, Minas Gerais, Brazil*

(Received 5 July 2021; revised 10 September 2021; accepted 20 September 2021; published 30 September 2021)

In this work, we investigated magnetotransport properties in epitaxial heterostructure of SnTe/$Sn_{1-x}Eu_xTe$ under dark and infrared light illumination. The longitudinal resistance has indicated the presence of Shubnikov–de Haas oscillations in the temperature range of 1.9–30 K. The fast Fourier transform analysis, performed under light and dark conditions, enabled us to understand the magnetotransport mechanism through the individual layers, leading to the proper address of each frequency that compound the Shubnikov–de Haas oscillations.

DOI: 10.1103/PhysRevB.104.125203

I. INTRODUCTION

Topological insulators (TIs) have been widely investigated in the last years due to the interesting quantum properties arising from the presence of strong spin-orbit coupling and time-reversal symmetry (TRS) [1,2], which gives origin to gapless metallic surface states. This quantum phase has attracted great interest for a new field in condensed matter. Since these topological states imply the study of protected band symmetries, novel TIs classifications are being added, such as for magnetic topological states protected by lattice translation and crystalline insulators with mirror symmetries [3–6]. The latter has contributed to studies in topological crystalline insulators (TCIs) which are applied to spintronics and quantum computation devices [7–10].

The topological crystalline phase was first predicted by Fu *et al.* [9] in a theoretical study of a tetragonal crystal (001) surface. The tight-binding model calculations, associated with TRS with and crystal fourfold symmetry, lead to the emergency search for crystalline insulators in IV-VI semiconductors. Later on, Hsieh *et al.* [5] demonstrated that tin telluride (SnTe) has an inverted intrinsic band at the four L Brillouin zone points, implying a nontrivial insulator topology. Thereby, the SnTe materials have shown to have an even number of Dirac cones in {001}, {110}, and {111} planes, which makes this class of SnTe materials applicable in TCI research.

Experimentally, the TCIs were initially observed in angle-resolved photoemission spectroscopy by Tanaka [11], which revealed the presence of Dirac cone in $\bar{X}$ point of the Brillouin zone, along $\bar{\Gamma}\bar{X}$ direction of SnTe (001) surface. Also, SnTe compounds such as $Pb_{1-x}Sn_xTe$ [12,13] and $Pb_{1-x}Sn_xSe$ [14], in addition its heterostructures [15], are reported as TCIs, where a transition from semiconductor state to crystalline topological insulator is observed for a given x concentration. Also, some works suggest that the introduction of dopants elements, like Bi and In-Doped SnTe, could diminish the disorders from the bulk band and improve topological surface states (TSS) [16,17]. To determine whether the bulk or TSS contribute to electrical transport, magnetotransport with angle dependence measurements are usually performed and enable a systematic study of Shubnikov–de Haas and de Haas–van Alphen effects [18]. Previous research of experimentally works with SnTe and Eu content are limited to very few papers. Structural property investigation of SnTe/$Sn_{1-x}Eu_xTe$ superlattices was analyzed [19], while electrical characterization of $Sn_{1-x}Eu_xTe$ was performed, and a sharp film degradation was observed for $x > 0.03$ [20]. In addition, already for $x > 0.014$, samples present antiferromagnetic phase for temperatures below 10 K, due to the formation of EuTe clusters [21]. It was also verified, from computational studies, that an Eu content present in SnSe/EuS heterostructure enables a nonzero gap at the Dirac point of the linear dispersion relation [22]. In the case of SnTe/$Sn_{1-x}Eu_xTe$ heterostructure investigated in this work, the SnTe grown on BaF_2 acts as a buffer layer in order to accommodate completely the 2% lattice mismatch [19]. This reduces the scattering due to defects and enhances the carrier mobility making possible the observation of Shubnikov–de Haas (SdH) oscillations at lower magnetic fields.

To study magnetotransport in the crystalline topological insulator SnTe/$Sn_{1-x}Eu_xTe$ heterostructure with $x \sim 0.02$, a magnetic field was applied up to 9 T for temperatures ranging from 1.9 to 30 K. In this temperature range, SdH oscillation patterns above 5 T were observed. To understand the origin of these oscillations the two main peaks of the fast Fourier transform (FFT) were analyzed using angular dependence of the SdH oscillations as a function of the inverse of perpendicular magnetic field $(1/B\cos\theta)$. These angle evolution considerations were not sufficient to assume the existence of bulk states or TSS, since the SnTe Fermi bulk carrier ellipsoidal

*Corresponding author: marcelos@unifei.edu.br

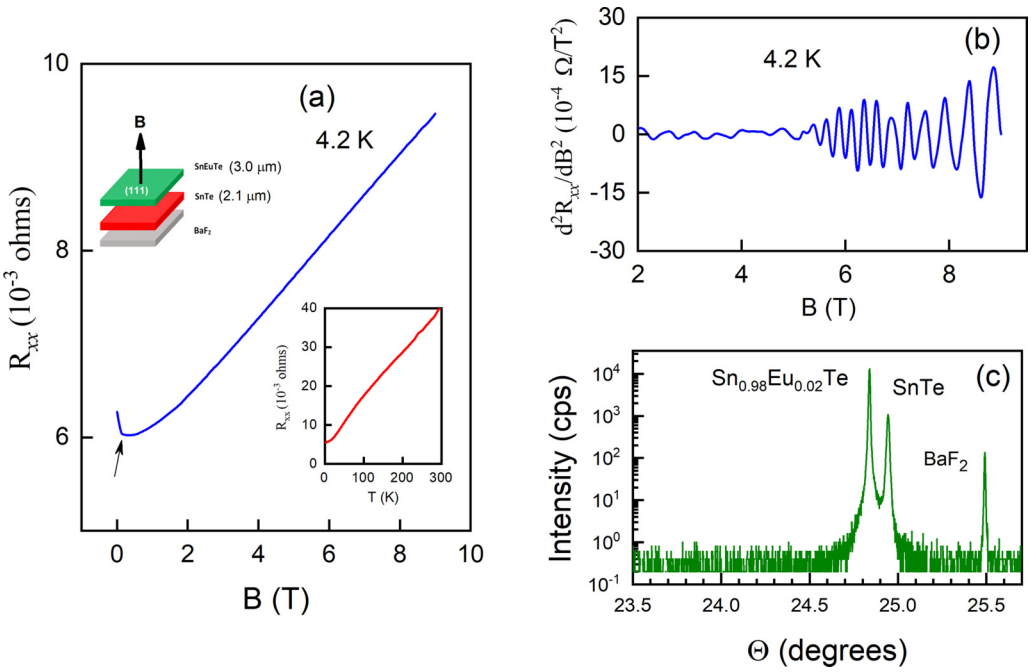

FIG. 1. (a) Longitudinal resistance (R_{xx}) as a function of magnetic field (B) at a temperature of 4.2 K for the SnTe/$Sn_{0.98}Eu_{0.02}Te$ heterostructure. The top inset shows a schematic representation of the heterostructure with the layers grown in the same direction (111) as the magnetic field B. The bottom inset shows R_{xx} as a function of the 1.9–300 K temperature range. (b) The second derivative of R_{xx} as a function of B, showing the presence of clear Shubnikov–de Haas oscillations. (c) X-ray diffraction pattern for SnTe/$Sn_{0.98}Eu_{0.02}Te$ heterostructure grown on BaF_2 substrate.

pocket also has shown to correspond to $1/\cos\theta$. The fitting performed on the amplitude curve of the SdH oscillations, using the Lifshitz-Kosevich expression, could not reveal any contribution from TSS. In addition, we found that when the sample is illuminated with infrared (IR) light, it is possible to identify the contribution of SnEuTe layer to the FFT peaks.

II. EXPERIMENT

In this work, we investigate the magnetotransport properties in a heterostructure, formed by a SnTe layer, directly seated on a {111} cleaved barium fluoride (BaF_2) substrate, and by a $Sn_{0.98}Eu_{0.02}Te$ cap layer, totaling a thickness of 5.11 μm. The SnTe and $Sn_{1-x}Eu_xTe$ layers were grown by the molecular beam epitaxy technique, at a temperature of 300 °C, with 2.1 and 3.0 μm thick, respectively, and a growth rate of approximately 1 μm/h. The SnTe effusion cell had the temperature fixed at 690 °C, giving a beam equivalent pressure (BEP) of 8.5×10^{-7} Torr. For Eu-doped SnTe film the effusion cell temperature used was 318 °C, with BEP 0.17×10^{-7} Torr for Eu content. High-resolution x-ray diffraction measurement was carried out in a Philips X'Pert diffractometer. The scans were measured around the (222) Bragg diffraction peak. The sample contacts were prepared by soldering Au wires with indium pellets on the sample surface following the Van der Pauw geometry. Magnetotransport measurements, with magnetic field up to 9 T, were performed in a ^{4}He cryostat using the equipment Physical Property Measurement System (PPMS) from Quantum Design, using the standard four-probe AC lock-in technique with a constant excitation current of 10 μA. The optical excitation was provided by an infrared light-emitting diode with a peak wavelength of 940 nm and 12 mW/m^2 and constant excitation current of 6 mA.

III. RESULTS AND DISCUSSION

Figure 1(a) shows the longitudinal resistance (R_{xx}) as a function of the magnetic field B, applied perpendicularly to the (111) direction of the sample surface at 4.2 K [see upper inset of Fig. 1(a)]. At lower fields, $B < 1$ T, the SnTe/$Sn_{0.98}Eu_{0.02}Te$ sample shows a weak localization effect (see arrow), which is expected in metallic systems with small disorder [23]. For higher fields, a magnetoresistance curve exhibits monotonic and linear behavior with field increase up to 9 T. The inset at the bottom of Fig. 1(a) shows that the sample exhibits metallic behavior across the entire measured temperature range (1.9–300 K).

To remove the linear dependence and the background, we perform the second derivative of the longitudinal resistance with respect to the magnetic field, (d^2R_{xx}/dB^2), as shown in Fig. 1(b). This figure clearly shows the presence of Shubnikov–de Haas oscillations for $B > 5$ T in the SnTe/$Sn_{0.98}Eu_{0.02}Te$ sample and the beat patterns show the existence of oscillatory frequency components, which are attributed to the Fermi surface pocket cross-sections. The presence of Shubnikov–de Haas also indicates the high carrier mobility of the sample due to the high crystalline quality. Figure 1(c) shows high-resolution x-ray diffractogram. It can be seen that a good crystal quality is achieved. The peaks of SnTe and $Sn_{0.98}Eu_{0.02}Te$ are clearly seen in the spectra due to

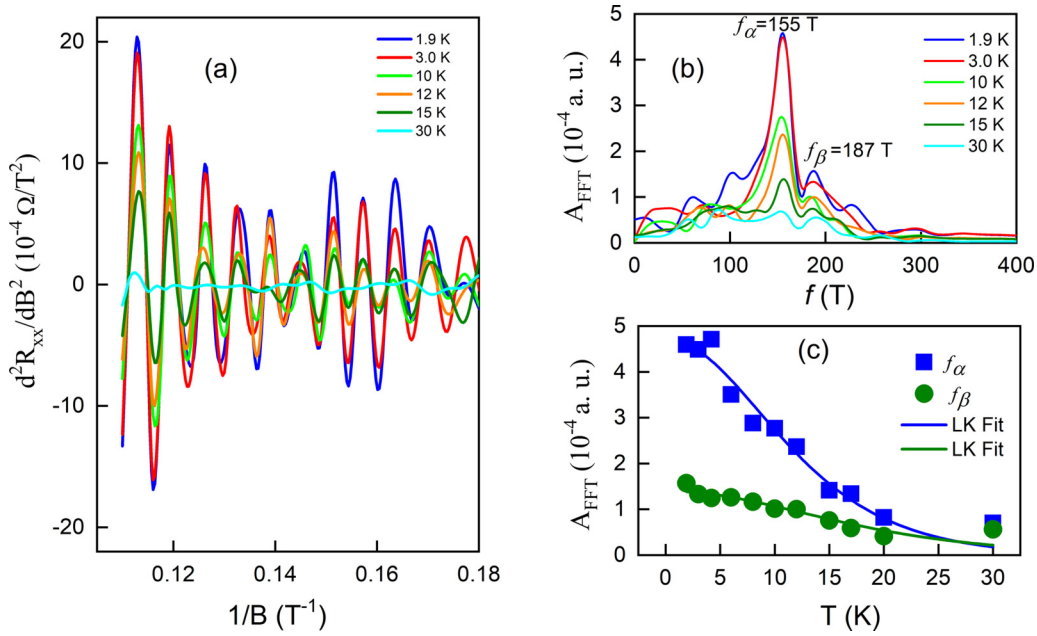

FIG. 2. The second derivative of longitudinal resistance as a function of the inverse of magnetic field and its fast Fourier transform (FFT) analyzes are represented in (a) and (b), respectively, varying the temperature below 30 K. In (c) the fitting curves for FFT amplitudes, in a range of 1.9–30 K, corresponding to f_α (blue squares) and f_β (green circles).

their different lattice constants. Also one can observe the peak of BaF_2 substrate.

For further analysis, we performed additional magnetoresistance measurements in a temperature range of 1.9–30 K. Figure 2(a) shows the second derivate of resistivity, d^2R_{xx}/dB^2, as a function of the inverse of the magnetic field. As expected, the amplitude of the oscillations is suppressed as the temperature increases due to the broadening of Landau levels. The amplitudes in Fig. 2(a) are attenuated as the temperature is raised, obeying the Lifshitz-Kosevich (LK) thermodynamic term,

$$A_{\mathrm{FFT}} = A_0\left(\frac{2\,\pi\,k_B}{e\,\hbar}\,\frac{m^{\mathrm{cyc}}\,T}{\bar{B}}\right)\Big/\,\sinh\left(\frac{2\,\pi\,k_B}{e\,\hbar}\,\frac{m^{\mathrm{cyc}}\,T}{\bar{B}}\right), \quad (1)$$

where the parameters A_0, $\hbar$, k_B, e, and $\bar{B}$ are the constant of adjustment, reduced Planck constant, Boltzmann constant, elementary electrical charge, and effective magnetic field, respectively. The last parameter, $\bar{B}$, is the mean value of the inverse of $1/B$, which is an interval parameter, used to extract the FFT curves. For this purpose, we considered an interval of 0.11 T^{-1} (9 T) to 0.18 T^{-1} (5.5 T), which also allowed us to calculate the cyclotronic mass.

To extract the frequency components responsible for the SdH oscillations, we have performed FFT analysis on the curves shown in Fig. 2(a). The FFT amplitudes enabled to distinguish two main frequencies at $f_\alpha = 155$ T and $f_\beta = 187$ T as shown in Fig. 2(b). The other peaks are discarded as they do not follow the standard temperature dependence behavior. From these frequencies, we can calculate the carrier concentration by the relation $p = {k_{Fa}}^2 k_{Fb}/3\pi^2$, where k_{Fa} and k_{Fb} are the Fermi wave vectors due to the semiminor axis (a) and semimajor axis (b), respectively, of the longitudinal ellipsoid pocket of the SnTe [24]. For SnTe, taking into account anisotropy of the Fermi pocket, $\frac{k_{Fb}}{k_{Fa}} = 2.9$ and $k_{Fa} = (2ef/\hbar)^{\frac{1}{2}}$, the total hole concentration obtained from the SdH frequencies is $p_{\mathrm{SdH}} = p(f_\alpha) + p(f_\beta) + 3p(f_o)$, where $f_o = 2.1 f_\alpha$, considering f_α originated from the longitudinal valley, is the contribution from the oblique ellipsoid [23] which was not detected in the FFT analysis. Also, the multiplicative factor 3 corresponds to three oblique valleys in the Fermi surface. The result is $p_{\mathrm{SdH}} = 3.63\times10^{20}$ cm^{-3}, a close value when compared to the carrier concentration obtained by means of Hall measurements at 4.2 K, $p_{\mathrm{Hall}} = (3.32 \pm 0.01)\times10^{20}$ cm^{-3}.

The solid blue and green lines in Fig. 2(c) are the fittings performed using Eq. (1), while the squared (f_α) and circle (f_β) points are the amplitudes taken from Fig. 2(b). The extracted cyclotronic masses are $m_\alpha^{\mathrm{cyc}} = (0.089 \pm 0.005)m_e$ and $m_\beta^{\mathrm{cyc}} = (0.061 \pm 0.006)m_e$, with the free-electron mass unit expressed by m_e. These values are close to those found in the literature for SnTe films [24–26]. It is important to point out that, so far, it is not possible to address the parameters obtained to specific layers of the $SnTe/Sn_{0.98}Eu_{0.02}Te$ heterostructure.

The electrical transport in the sample, investigated here, occurs via SnTe and $Sn_{0.98}Eu_{0.02}Te$ layers, so that the oscillations may be due to the contribution from both layers. Therefore, it is important to identify the contribution of each layer to magnetotransport. Under illumination, photogenerated carriers can change the carrier concentration within the layers, which will depend on the penetration depth, γ, of the light. For this reason, the sample was exposed to IR radiation to verify the contribution of each layer to the oscillation patterns. Figure 3(a) shows a diagram that represents the sample illuminated by IR light, where the penetration depth can be calculated by the relation $\gamma = \sqrt{\lambda/\pi c\mu_0\sigma}$, where λ is the

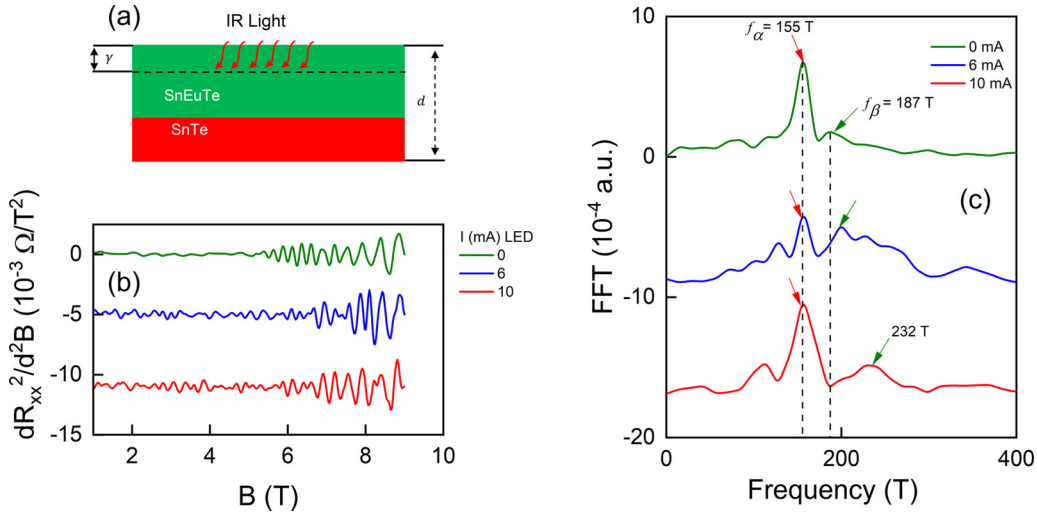

FIG. 3. (a) Schematic representation of the SnTe/$Sn_{1-x}Eu_x$Te transversal cross section indicating the penetration depth of infrared radiation by $\boldsymbol{\gamma}$. In (b), we observe the decrease in the beat patterns of the second derivatives of R_{xx} as a function of the magnetic field as the current in the infrared LED increases in a range from 0 to 10 mA. (c) The FFT curves for each curve shown in (b) for different LED intensities.

wavelength of the light, σ is the electrical conductivity of the layer, μ_0 is the magnetic permeability of the free space, and c is the speed of the light in space. We found $\gamma \approx 3.8$ nm, which is three orders of magnitude smaller than the thickness of the top layer of $Sn_{0.98}Eu_{0.02}Te$ (3.1 μm). This indicates that light penetrates only a small depth into the $Sn_{0.98}Eu_{0.02}Te$ layer and therefore, under illumination, only the $Sn_{0.98}Eu_{0.02}Te$ layer could be responsible for the contribution of the photogenerated carriers.

Figure 3(b) shows d^2R_{xx}/dB^2 as a function of B in the dark and under illumination for different light intensities when the LED current ranges from 0 to 10 mA (note that light intensity emitted is proportional to the current applied through the LED) at 4.2 K. In this figure, it can be seen that the oscillation for different light intensities does not change considerably. However, for low magnetic fields, oscillation amplitudes are overcome by the appearance of background noise. Figure 3(c) shows the FFT spectra of the SdH oscillations shown in Fig. 3(b). As the light intensity increases, peak f_α remains in the same position, while f_β shifts to higher frequencies (see arrows). Therefore, as the position of f_α does not change with the light intensity, we suggest that this frequency comes from the longitudinal ellipsoid of SnTe, while f_β comes from the longitudinal ellipsoid of $Sn_{0.98}Eu_{0.02}Te$, since this layer is partially penetrated by light radiation. In SdH oscillations, it is known that the frequency is proportional to the carrier concentration, according to $p = (2.9/3\pi^2)(2e/\hbar)^{3/2} f^{3/2}$. Hall measurements show that the carrier concentration of SnTe/$Sn_{0.98}Eu_{0.02}Te$ heterostructure is higher under LED illumination. That is, for a luminous intensity corresponding to a current of 10 mA, the carrier concentration ($p^{\text{on}}_{\text{Hall}} = (3.40 \pm 0.01)\times 10^{20}$ cm^{-3}) is greater than its value in the dark condition ($p^{\text{off}}_{\text{Hall}} = (3.32 \pm 0.01)\times 10^{20}$ cm^{-3}). Thus, when the sample is illuminated, electrons and holes are photogenerated leading to an increase in the carrier concentration and, consequently, changing the oscillation frequency only in the $Sn_{0.98}Eu_{0.02}Te$ layer.

To investigate whether SdH oscillations originate from bulk or topological surface states of SnTe and $Sn_{0.98}Eu_{0.02}Te$ layers, we performed angle-dependent measurements of R_{xx}. In Fig. 4(a), we present the second derivative of R_{xx} as a function of $1/(B\cos\theta)$, for tilt angles θ ranging from 0° to 40°. The sample is rotated *in situ* while the magnetic field is kept in a fixed direction. The field component perpendicular to the sample surface makes an angle θ with the fixed direction (see inset). The dashed lines show the maxima aligned in the same position for all angles, indicating the possibility of the 2D nature, originated from the Fermi surface states, of the SdH oscillations. As the magnetic field is rotated, the SdH oscillation patterns systematically evolve and the amplitude of the oscillations decreases. For these oscillation curves, two main frequencies were also calculated in the FFT analysis and the frequencies follow the dependence of the $1/\cos\theta$ up to 40°, as shown by the solid lines in Fig. 4(b).

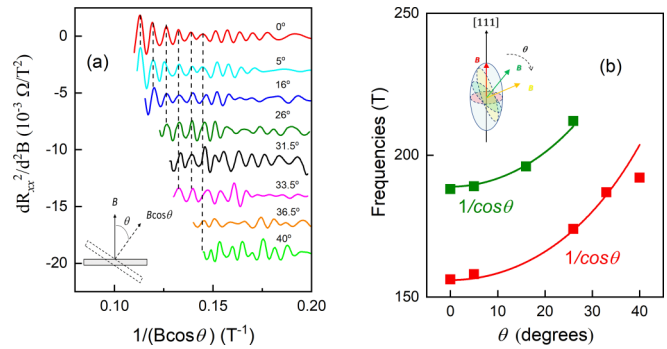

FIG. 4. (a) Second derivative of R_{xx} with respect to B as a function of $1/B$, showing the angular dependence of the applied magnetic field between 0° and 40°. FFT analyses of the curves in graph (a) display two main frequency ranges that are related in graph (b) by $1/\cos\theta$. The inset in (b) is a pictorial illustration of a Fermi surface, in this case, SnTe in the direction (111), correlating the hatch cross-section areas that increase as the direction of the magnetic field changes.

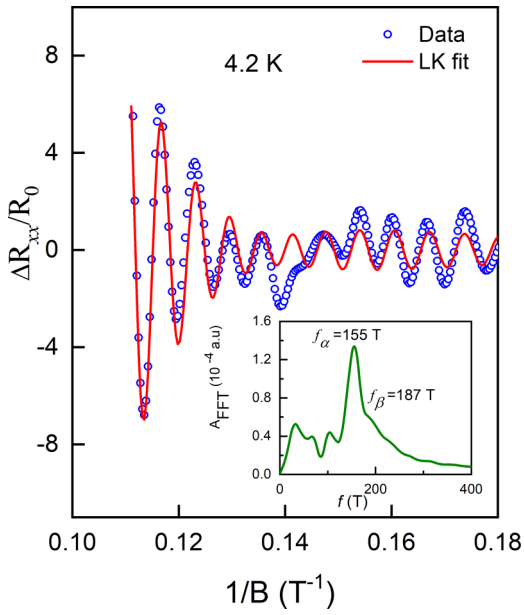

FIG. 5. Normalized beat pattern oscillations $\Delta R_{xx}/R_0$ of experimental data obtained by subtraction of a third-order polynomial (blue circles) and represented in a solid red line is the Lifshitz-Kosevich (LK) expression given by Eq. (2). The FFT curve for ΔR_{xx} obtained from the background subtraction is shown in the inset.

For some time, $1/\cos\theta$ dependence of the frequency was indicative of transport via, topological surface states, in TIs structures [26–28], indicating the possible two-dimensional (2D) nature of quantum oscillations. In this case, Fig. 4(b) would suggest the presence of surface states in SnTe/$Sn_{0.98}Eu_{0.02}Te$ sample. However, the angular dependence $1/\cos\theta$ presented by the frequency of the SdH oscillations is not sufficient to assure conduction via surface states. Bulk SnTe alloy has elongated Fermi ellipsoids [see inset of Fig. 4(b)], so the cyclotron frequency must follow the same $1/\cos\theta$ dependence, as expected for the 3D bulk Fermi surface. Therefore, from this analysis, we cannot distinguish whether the observed SdH oscillations originate from normal bulk fermions or surface Dirac fermions.

Further evidence for the origin of SdH oscillations from topological surface states is the proper analysis of the Berry phase. A nontrivial Berry phase is expected for the Dirac fermions. For the analysis, a third-order polynomial fit is subtracted from the magnetoresistance curve of R_{xx}, shown in Fig. 1(a). The inset of Fig. 5 shows the FFT of the ΔR_{xx} obtained from the subtraction. One can observe that the two frequencies obtained are the same as f_α and f_β exhibited in Fig. 1 (b). This result confirms that ΔR_{xx} was derived properly from the background subtraction. After subtraction, we fit the normalized oscillatory component $\Delta R_{xx}/R_0$ as a function of the inverse of the magnetic field with the complete LK expression:

$$\frac{\Delta R_{xx}}{R_0} = \sqrt{\frac{\hbar\omega_c}{2\varepsilon_F}}\,\frac{\lambda}{\sinh\lambda}\,e^{-\lambda_D}\,\cos\left[2\pi\left(\frac{\varepsilon_F}{\hbar\omega_c}+\frac{1}{2}+\varphi\right)\right], \tag{2}$$

where $\varepsilon_F = (\hbar\, k_F)^2/2\, m^{cyc}$, k_F is the Fermi wave vector, $\omega_c = e\,B/m^{cyc}$ is the cyclotron frequency, λ and λ_D are expressed as $\lambda = 2\,\pi^2 k_B T\ /\hbar\,\omega_c$ and $\lambda_D = 2\,\pi^2 k_B T_D\ /\hbar\,\omega_c$. T_D is the Dingle temperature which is related to the quantum mobility by $\mu = e\hbar/2\pi m k_B T_D$. The phase parameter $\varphi = \beta - \delta$ gives the dimensionality of the Fermi surface, where β is directly proportional to the Berry phase and δ to the Fermi surface dimension [29]. For transport with trivial fermions, β values can assume values in the range 0 to 1, while Dirac fermions are defined for $\beta = 1/2$ [30]. In addition, $\delta = 0$ indicates that the Fermi surface is 2D, while $\delta = -1/8$ or $+1/8$ indicates the Fermi surface is 3D [31].

Figure 5 shows the normalized amplitude of the SdH oscillations $\Delta R_{xx}/R_0$, where R_0 is the resistance at zero magnetic field, as a function of $1/B$ (blue circles) together with the best fitting, considering a sum of two expressions given by Eq. (2) (solid red line), at 4.2 K. T_D, frequencies oscillation components (f), and phase parameter φ were considered as free parameters and the temperature T was fixed at 4.2 K. For the fitting, the cyclotron masses calculated in Fig. 2(c) were used. The best-fit parameters obtained were $f_1 = 149$ T, $f_2 = 153$ T, $\beta_1 - \delta = 0.85 \pm 0.01$ and $\beta_1 - \delta = 0.80 \pm 0.01$. The phase values are very close to $1 \pm 1/8$ corresponding to a trivial Berry phase. The frequencies f_1 and f_2 obtained in the LK fitting are close to the f_α extracted from the FFT analysis. The FFT analysis shows that the SdH oscillations are composed of two frequencies ($f_\alpha = 155$ T and $f_\beta = 187$ T), however, the LK fit was unsuccessful with f_β being included. Since f_β is related to the $Sn_{0.98}Eu_{0.02}Te$ layer, we believe that this is because Eu doping reduces the mobility of carriers in this layer. The values found for $T_{D1} = 32.8$ K and $T_{D2} = 31.7$ K led to the respective mobilities $\mu_1 = 1512$ cm^2(Vs)$^{-1}$ and $\mu_2 = 1567.7$ cm^2(Vs)$^{-1}$ that are close to the values in the literature [25,32].

Since f_1 and f_2 are very close to f_α we believe that f_1 and f_2 are not resolved in the FFT curves shown in Fig. 2 (b). Hence, the observed frequency in the FFT analysis $f_\alpha = 155$ T is actually a composition of these two close peaks. These frequencies can be originated from the Rashba effect, previously observed in the SnTe film [33]. From f_1 and f_2 we obtain the Fermi wave vectors $k_{F1} = 0.067$ Å^{-1} and $k_{F2} = 0.068$ Å^{-1}. The Fermi velocity $v_F = \hbar k_F/m^{cyc}$ calculated from these values are $v_{F1} = 8.75\times10^5$ m/s and $v_{F2} = 8.9\times10^5$ m/s, are close to the values found in the literature for SnTe films [24]. The Rashba splitting in momentum space, Δk_R, can be calculated from geometric considerations taking into account the distance between the center of the two circles leading to the value of $\Delta k_R \sim 0.001$ Å^{-1}. Then the Rashba energy, $E_R = \hbar^2 \Delta {k_R}^2/2m_c = 0.17$ meV, and the Rashba parameter $\alpha_R = 2E_R/\Delta k_R = 0.17$ eV Å^{-1} is obtained. These values found for Δk_R, α_R and E_R are a minor order of those in literature [24,34,35].

IV. CONCLUSIONS

In this work, we present the magnetotransport measurements performed on the SnTe\ $Sn_{0.98}Eu_{0.02}Te$ heterostructure in the temperature range 1.9–30 K, and magnetic field up to 9 T, and we found clear SdH oscillations. We used IR light to properly address the contribution of each layer of

the heterostructure and were able to identify two different frequencies belonging to each layer. From the frequencies, carrier concentration and cyclotronic masses were calculated. Angular dependence measurements and computer simulation of the LK equation revealed that no significant contribution from topological surface states is detected in the electrical transport. In addition, from the computer simulation, we found that the FFT peak corresponding to the SnTe layer is actually a composition of two frequencies and we sugest that this composition results from Rashba effect.

ACKNOWLEDGMENT

We thank CAPES and CNPq (Grant No. 305764/2018-7) for their financial support.

[1] M. Z. Hasan and C. L. Kane, Colloquium: topological insulators, Rev. Mod. Phys. **82**, 3045 (2010).

[2] X. L. Qi and S. C. Zhang, The quantum spin hall effect and topological insulators, Phys. Today **63**, 33 (2010).

[3] Y. Tokura, K. Yasuda, and A. Tsukazaki, Magnetic topological Insulators, Nat. Rev. Phys. **1**, 126 (2019).

[4] R. S. K. Mong, A. M. Essin, and J. E. Moore, Antiferromagnetic topological insulators, Phys. Rev. B **81**, 245209 (2010).

[5] T. H. Hsieh, H. Lin, J. Liu, W. Duan, A. Bansil, and L. Fu, Topological crystalline insulators in the SnTe material class, Nat. Commun. **3**, 982 (2012).

[6] J. Liu, W. Duan, and L. Fu, Two types of surface states in topological crystalline insulators, Phys. Rev. B **88**, 241303(R) (2013).

[7] J. Liu, T. H. Hsieh, P. Wei, W. Duan, J. Moodera, and L. Fu, Spin-filtered edge states with an electrically tunable gap in a two-dimensional topological crystalline insulator, Nat. Mater. **13**, 178 (2014).

[8] I. Zeljkovic, D. Walkup, B. A. Assaf, K. L. Scipioni, R. Sankar, F. Chou, and V. Madhavan, Strain engineering dirac surface states in heteroepitaxial topological crystalline insulator thin films, Nat. Nanotech. **10**, 849 (2015).

[9] M. Safdar, Q. Wang, M. Mirza, Z. Wang, K. Xu, and J. He, Topological surface transport properties of single-crystalline snte nanowire, Nano Lett. **13**, 5344 (2013).

[10] K. Zou, S. D. Albright, O. E. Dagdeviren, M. D. Morales-Acosta, G. H. Simon, C. Zhou, S. Mandal, S. Ismail-Beigi, U. D. Schwarz, E. I. Altman, F. J. Walker, and C. H. Ahn, Revealing surface-state transport in ultrathin topological crystalline insulator SnTe films, APL Mater. **7**, 051106 (2019).

[11] Y. Tanaka, Z. Ren, T. Sato, K. Nakayama, S. Souma, T. Takahashi, K. Segawa, and Y. Ando, Experimental realization of a topological crystalline insulator in SnTe, Nat. Phys. **8**, 800 (2012).

[12] S. Safaei, P. Kacman, and R. Buczko, Topological crystalline insulator (Pb,Sn)Te: surface states and their spin polarization, Phys. Rev. B **88**, 045305 (2013).

[13] S. Y. Xu, C. Liu, N. Alidoust, M. Neupane, D. Qian, I. Belopolski, J. D. Denlinger, Y. J. Wang, H. Lin, L. A. Wray, G. Landolt, B. Slomski, J. H. Dil, A. Marcinkova, E. Morosan, Q. Gibson, R. Sankar, F. C. Chou, R. J. Cava, A. Bansil, and M. Z. Hasan, Observation of a topological crystalline insulator phase and topological phase transition in $Pb_{1-x}Sn_xTe$, Nat. Commun. **3**, 1192 (2012).

[14] P. Dziawa, B. J. Kowalski, K. Dybko, R. Buczko, A. Szczerbakow, M. Szot, E. Łusakowska, T. Balasubramanian, B. M. Wojek, M. H. Berntsen, O. Tjernberg, and T. Story, Topological crystalline insulator states in $Pb_{1-x}Sn_xSe$, Nat. Mater. **11**, 1023 (2012).

[15] R. Buczko and L. Cywiński, PbTe/PbSnTe heterostructures as analogs of topological insulators, Phys. Rev. B **85**, 205319 (2012).

[16] Y. Zou, Z. Chen, F. Kong, E. Zhang, J. Drennan, K. Cho, F. Xiu, and J. Zou, Surface-energy engineered bi-doped SnTe nanoribbons with weak antilocalization effect and linear magnetoresistance, Nanoescale **8**, 19383 (2016).

[17] C. M. Polley, V. Jovic, T. Y. Su, M. Saghir, D. Newby, B. J. Kowalski, R. Jakiela, A. Barcz, M. Guziewicz, T. Balasubramanian, G. Balakrishnan, J. Laverock, and K. E. Smith, Observation of surface states on heavily indium-doped SnTe(111), a superconducting topological crystalline insulator, Phys. Rev. B **93**, 075132 (2016).

[18] K. Dybko, M. Szot, A. Szczerbakow, M. U. Gutowska, T. Zajarniuk, J. Z. Domagala, A. Szewczyk, T. Story, and W. Zawadzki, Experimental evidence for topological surface states wrapping around a bulk SnTe crystal, Phys. Rev. B **96**, 205129 (2017).

[19] E. Abramof, P. H. O. Rappl, and A. Y. Ueta, High-resolution X-Ray diffraction analysis of $SnTe/Sn_{1-x}Eu_xTe$ superlattices grown on (111) BaF_2 substrates, Physica E **20**, 462 (2004).

[20] A. Y. Ueta, P. H. O. Rappl, H. Closs, P. Motisuke, E. Abramof, V. R. Anjos, V. A. Chitta, J. A. Coaquira, N. F. O. Jr, and G. Bauer, MBE growth and characterization of $Sn_{1-x}Eu_xTe$, Braz, J. Phys. **34**, 672 (2004).

[21] M. Górska, J. R. Anderson, J. L. Peng, and Z. Gołacki, Magnetization and susceptibility of $Sn_{1-x}Eu_xTe$: Eu Te, J. Phys. Chem. Solids **56**, 1253 (1995).

[22] S. Yang, C. Wu, and N. Marom, Topological properties of SnSe/EuS and SnTe/CaTe interfaces, Phys. Rev. Mater. **4**, 034203 (2020).

[23] M. Safdar, Q. Wang, Z. Wang, X. Zhan, K. Xu, F. Wang, M. Mirza, and J. He, Weak antilocalization effect of topological crystalline insulator $Pb_{1-x}Sn_xTe$ nanowires with tunable composition and distinct {100} facets, Nano Lett. **15**, 2485 (2015).

[24] A. K. Okazaki, S. Wiedmann, S. Pezzini, M. L. Peres, P. H. O. Rappl, and E. Abramof, Shubnikov–de Haas oscillations in topological crystalline insulator SnTe(111) epitaxial films, Phys. Rev. B **98**, 195136 (2018).

[25] A. A. Taskin, F. Yang, S. Sasaki, K. Segawa, and Y. Ando, Topological surface transport in epitaxial SnTe thin films grown on Bi_2Te_3, Phys. Rev. B **89**, 121302(R) (2014).

[26] C. Zhang, X. G. He, H. Chi, R. Zhong, W. Ku, G. Gu, J. M. Tranquada, and Q. Li, Electron and hole contributions to normal-state transport in the superconducting system $Sn_{1-x}In_xTe$, Phys. Rev. B **98**, 054503 (2018).

[27] A. Dankert, P. Bhaskar, D. Khokhriakov, I. H. Rodrigues, B. Karpiak, M. V. Kamalakar, S. Charpentier, I. Garate, and S. P. Dash, Origin and evolution of surface spin current in topological insulators, Phys. Rev. B **97**, 125414 (2018).

[28] E. Lahoud, E. Maniv, M. S. Petrushevsky, M. Naamneh, A. Ribak, S. Wiedmann, L. Petaccia, Z. Salman, K. B. Chashka, Y. Dagan, and A. Kanigel, Evolution of the fermi surface of a doped topological insulator with carrier concentration, Phys. Rev. B **88**, 195107 (2013).

[29] L. P. He, X. C. Hong, J. K. Dong, J. Pan, Z. Zhang, J. Zhang, and S. Y. Li, Quantum Transport Evidence for the Three-Dimensional Dirac Semimetal Phase in Cd_3As_2, Phys. Rev. Lett. **113**, 246402 (2014).

[30] Z. Ren, A. A. Taskin, S. Sasaki, K. Segawa, and Y. Ando, Large bulk resistivity and surface quantum oscillations in the topological insulator Bi_2Te_2Se, Phys. Rev. B **82**, 241306(R) (2010).

[31] X. Liu, C. Yue, S. V. Erohin, Y. Zhu, A. Joshy, J. Liu, A. M. Sanchez, D. Graf, P. B. Sorokin, Z. Mao, J. Hu, and J. Wei, Quantum transport of the 2D surface state in a nonsymmorphic semimetal, Nano Lett. **21**, 4887 (2021).

[32] A. Ishida, T. Tsuchiya, T. Yamada, D. Cao, S. Takaoka, M. Rahim, F. Felder, and H. Zogg, Electrical and optical properties of SnEuTe and SnSrTe films, J. Appl. Phys. **107**, 123708 (2010).

[33] C. D. O'Neill, O. J. Clark, H. D. J. Keen, F. Mazzola, I. Marković, D. A. Sokolov, A. Malekos, P. D. C. King, A. Hermann, and A. D. Huxley, Changes of Fermi surface topology due to the rhombohedral distortion in SnTe, Phys. Rev. B **102**, 155132 (2020).

[34] E. Plekhanov, P. Barone, D. Di Sante, and S. Picozzi, Engineering relativistic effects in ferroelectric SnTe, Phys. Rev. B **90**, 161108(R) (2014).

[35] V. V. Volobuev, P. S. Mandal, M. Galicka, O. Caha, J. Sánchez-Barriga, D. Di Sante, A. Varykhalov, A. Khiar, S. Picozzi, G. Bauer, P. Kacman, R. Buczko, O. Rader, and G. Springholz, Giant Rashba splitting in $Pb_{1-x}Sn_xTe$ (111) topological crystalline insulator films controlled by Bi doping in the bulk, Adv. Mater. **29**, 1604185 (2017).